GEOPHYSICS, VOL. 73, NO. 6 (NOVEMBER-DECEMBER 2008); P. S241–S249, 9 FIGS.
10.1190/1.2993536

The finite-frequency sensitivity kernel for migration residual moveout and its applications in migration velocity analysis

Xiao-Bi Xie[1] and Hui Yang[1]

ABSTRACT

We have derived a broadband sensitivity kernel that relates the residual moveout (RMO) in prestack depth migration (PSDM) to velocity perturbations in the migration-velocity model. We have compared the kernel with the RMO directly measured from the migration image. The consistency between the sensitivity kernel and the measured sensitivity map validates the theory and the numerical implementation. Based on this broadband sensitivity kernel, we propose a new tomography method for migration-velocity analysis and updating — specifically, for the shot-record PSDM and shot-index common-image gather. As a result, time-consuming angle-domain analysis is not required. We use a fast one-way propagator and multiple forward scattering and single backscattering approximations to calculate the sensitivity kernel. Using synthetic data sets, we can successfully invert velocity perturbations from the migration RMO. This wave-equation-based method naturally incorporates the wave phenomena and is best teamed with the wave-equation migration method for velocity analysis. In addition, the new method maintains the simplicity of the ray-based velocity analysis method, with the more accurate sensitivity kernels replacing the rays.

INTRODUCTION

Seismic reflection surveys conducted on the earth's surface generate data that can be used in depth migration for imaging subsurface structures. Because of the lack of an accurate velocity model, the migration usually is calculated in an initial model, which often results in an incoherent image. The distorted image carries important information regarding the errors in the migration-velocity model. Migration-velocity analysis (MVA) links the incoherence in the image to errors in the model and uses this information to modify the initial model toward the optimal velocity model. This process simultaneously improves the quality of the image and the velocity model.

The information used in MVA is the migration residual moveout (RMO) in different common-image gathers (CIGs), e.g., the shot-index CIG, the offset-index CIG, and the angle-index CIG (e.g., Prucha et al., 1999; Mosher and Foster, 2000; Rickett and Sava, 2002; Xie and Wu, 2002; Sava and Fomel, 2003). A variety of methods have been developed for extracting information from the RMO in different CIGs and for converting this information into corrections for velocity-model updating. The parameterized methods (e.g., Al-Yahya, 1989; Liu and Bleistein, 1992; Mosher, et al., 2001) are stable and robust. However, these updating formulas are limited by 1D assumptions, and they cannot deal with models containing strong lateral variations. More sophisticated techniques use tomography inversion to update the velocity model. Based on the ray-tracing technique (e.g., Bishop et al., 1985; Stork, 1992), the RMO information is converted to the velocity correction through back projection along the rays.

Another automatic velocity-analysis tool is the differential-semblance optimization method, first developed for stacked surface data (Symes and Carazzone, 1991; Chauris and Noble, 2001) and later used in processing migrated data (Shen et al., 2003; Khoury et al., 2006). This method updates the velocity model by reducing the misfocusing in CIGs. Building a migration-velocity updating algorithm under the full-wave theory and including all of the dynamic and kinematic information in the image for the inversion should be very helpful. Several techniques are currently under development (Biondi and Symes, 2004; Sava and Biondi, 2004; Soubaras and Gratacos, 2007).

The most important part of MVA is converting the observed RMO into velocity corrections and back-projecting them into the model space for velocity updating. This practice has been dominated by ray-based techniques that assume an infinitely high-frequency bandwidth. When a band-limited seismic wave propagates through a complex region, often the rays poorly approximate the actual wavepaths (Woodward, 1992; Biondi, 2006). The sensitivity of finite-frequency signals to the velocity model has been investigated by re-

Manuscript received by the Editor 19 February 2008; revised manuscript received 28 May 2008; published online 14 November 2008.
[1]University of California, Santa Cruz Institute of Geophysics and Planetary Physics, Santa Cruz, California, U.S.A. E-mail: xie@pmc.ucsc.edu; hyang@pmc.ucsc.edu.

searchers working in earthquake seismology (Dahlen et al., 2000; Huang et al., 2000; Zhao et al., 2000; Dahlen, 2005; Chen et al., 2007), ocean acoustics (Skarsoulis and Cornuelle, 2004), and applied seismology (Luo and Schuster, 1991; Woodward, 1992; Vasco et al., 1995; Sava and Biondi, 2004; Spetzler and Snieder, 2004; Jocker et al., 2006; Buursink and Routh, 2007; Fliedner et al., 2007). Finite-frequency sensitivity kernels have been used to solve many tomography problems with great success.

The major obstacle that prevents this method from being used in MVA is that the finite-frequency sensitivity kernels are used mostly for transmitted or reflected waves propagating from a point source to a point receiver, and the information is extracted from the data domain (e.g., traveltime delays or amplitude fluctuations in seismograms). In seismic migration/imaging, the waves propagate from a source to a subsurface target. The waves are scattered from the target, then come to the receivers to form the seismic data in the time domain. Finally, the time-domain data are migrated back to the depth domain to generate the subsurface image. The velocity-model errors are carried by the migrated wavefield entering the image and are shown as inconsistencies in CIGs. Unlike dealing directly with the seismograms, the information regarding the velocity error must be extracted from the depth image instead of from the data. De Hoop et al. (2006) derive the sensitivity kernel for reflection waves based on the double square root (DSR) equation. The sensitivity kernel relates the RMO in an angle-domain CIG to the velocity-model errors. Based on this sensitivity kernel, they propose a velocity-analysis method for offset-domain prestack migration.

In this paper, based on the scattering theory, we derive the broadband sensitivity kernel, particularly for shot-record prestack depth migration (PSDM). This sensitivity kernel relates the observed RMO in the depth image to the velocity correction in the model. We then validate this sensitivity kernel by comparing it to the directly measured sensitivity map in depth migration. Based on the sensitivity kernel, we propose a new wave-equation-based tomography method for MVA. It is formulated for the shot-record PSDM and shot-index CIGs. Thus, expensive angle decomposition is not required. We use an efficient method based on a one-way wave equation, multiple-forward-scattering and single-back-scattering approximation for calculating the sensitivity kernel. Finally, we use synthetic data sets to test potential applications of this broadband sensitivity kernel in MVA.

THEORETICAL SENSITIVITY ANALYSIS FOR RMO IN SHOT-INDEX CIG

Assume a true velocity model $v_T(\mathbf{r})$ can be expressed as

$$v_T(\mathbf{r}) = v_0(\mathbf{r}) + \delta v(\mathbf{r}), \tag{1}$$

where $v_0(\mathbf{r})$ is an initial model reasonably close to $v_T(\mathbf{r})$ and $\delta v(\mathbf{r})$ is the unknown difference between the initial and the true velocity models. Here, $v_T(\mathbf{r})$ represents the real earth, where the seismic survey is conducted or, in a theoretical investigation, the velocity model used for generating synthetic data. In both cases, a source located at $\mathbf{r}_S$ generates a downgoing wave $u_D^T(\mathbf{r};\mathbf{r}_S,\omega)$, where ω is the frequency. After interacting with subsurface targets, the downgoing wave generates an upgoing scattered wavefield $u_U^T(\mathbf{r};\mathbf{r}_S,\omega)$, carrying the information about structures. In reality, both the true velocity and the target location are unknown.

We conduct migration in an initial model $v_0(\mathbf{r})$ and obtain a frequency-domain image:

$$I(\mathbf{r}_I,\mathbf{r}_S,\omega) = u_D^0(\mathbf{r}_I;\mathbf{r}_S,\omega)u_U^0(\mathbf{r}_I;\mathbf{r}_S,\omega)^*, \tag{2}$$

where $u_D^0(\mathbf{r};\mathbf{r}_S,\omega)$ and $u_U^0(\mathbf{r};\mathbf{r}_S,\omega)$ are the down- and upgoing waves calculated in the initial model, the asterisk denotes the complex conjugation, $u_U^0(\mathbf{r}_I;\mathbf{r}_S,\omega)^*$ is the frequency-domain equivalent of the time-reversed original reflection wave, and $\mathbf{r}_I$ is the image point. Because of the errors in the velocity model, the image point usually is shifted from the true target location $\mathbf{r}_T$ by

$$\mathbf{r}_{\mathrm{RMO}} = \mathbf{r}_I - \mathbf{r}_T, \tag{3}$$

where $\mathbf{r}_{\mathrm{RMO}}$ is the vector RMO. At $\mathbf{r}_I$, the phase difference between the images generated using the initial model and true-velocity model is

$$\delta\varphi(\mathbf{r}_I,\mathbf{r}_S,\omega) = \arg\left\{\frac{u_D^T(\mathbf{r}_I;\mathbf{r}_S,\omega)}{u_D^0(\mathbf{r}_I;\mathbf{r}_S,\omega)}\right\} + \arg\left\{\frac{u_U^T(\mathbf{r}_I;\mathbf{r}_S,\omega)^*}{u_U^0(\mathbf{r}_I;\mathbf{r}_S,\omega)^*}\right\}, \tag{4}$$

where arg denotes the angle of a complex variable. Using the Rytov approximation (e.g., Wu et al., 2006; Jocker et al., 2006), we have

$$\delta\varphi(\mathbf{r}_I,\mathbf{r}_S,\omega) = \mathrm{Im}\left\{\frac{U_D(\mathbf{r}_I;\mathbf{r}_S,\omega)}{u_D^0(\mathbf{r}_I;\mathbf{r}_S,\omega)} + \frac{U_U(\mathbf{r}_I;\mathbf{r}_S,\omega)^*}{u_U^0(\mathbf{r}_I;\mathbf{r}_S,\omega)^*}\right\}, \tag{5}$$

where $U_D(\mathbf{r}_I;\mathbf{r}_S,\omega)$ and $U_U(\mathbf{r}_I;\mathbf{r}_S,\omega)$ are scattering waves caused by the velocity perturbation $\delta v(\mathbf{r})$ and Im denotes the imaginary part of a complex variable.

The purpose of migration-velocity updating is to estimate the velocity perturbation $\delta v(\mathbf{r})$ based on the observed $\delta\varphi$ or its equivalents. To do this, we create a relationship between these two parameters. Using the scattering theory, the scattered wave U can be obtained as (e.g., Woodward, 1992; Jocker et al., 2006)

$$U_D(\mathbf{r}_I;\mathbf{r}_S,\omega) = 2S(\omega)\int_V k_0^2 m(\mathbf{r}')G_D(\mathbf{r}';\mathbf{r}_S,\omega)G(\mathbf{r}';\mathbf{r}_I,\omega)dV', \tag{6}$$

$$U_U(\mathbf{r}_I;\mathbf{r}_S,\omega)^* = 2S(\omega)\int_V k_0^2 m(\mathbf{r}')G_U^*(\mathbf{r}';\mathbf{r}_S,\omega)G(\mathbf{r}';\mathbf{r}_I,\omega)dV', \tag{7}$$

where $m(\mathbf{r}) = \delta v(\mathbf{r})/v_0(\mathbf{r})$, $k_0 = \omega/v_0(\mathbf{r})$, $S(\omega)$ is the source spectrum, G is the Green's function from the scatter to the image point, and G_D and G_U are Green's functions for source and scattered waves, respectively. All of these Green's functions are calculated in the initial model.

The spatial integral $\int_V dV'$ includes all regions with velocity perturbations. Substituting equations 6 and 7 into equation 5, we have the phase delay

$$\delta\varphi(\omega) = \delta\varphi_D(\omega) + \delta\varphi_U(\omega), \tag{8}$$

with $\delta\varphi_D(\omega)$ and $\delta\varphi_U(\omega)$ calculated as

$$\delta\varphi_D(\mathbf{r}_I,\mathbf{r}_S,\omega) = \int_V m(\mathbf{r}')K_D^F(\mathbf{r}',\mathbf{r}_S,\mathbf{r}_I,\omega)dV', \tag{9}$$

$$\delta\varphi_U(\mathbf{r}_I,\mathbf{r}_S,\omega) = \int_V m(\mathbf{r}')K_U^F(\mathbf{r}',\mathbf{r}_S,\mathbf{r}_I,\omega)dV', \quad (10)$$

where the integrands

$$K_D^F(\mathbf{r},\mathbf{r}_S,\mathbf{r}_I,\omega) = \mathrm{Im}\left[2k_0^2\frac{G_D(\mathbf{r};\mathbf{r}_S,\omega)G(\mathbf{r};\mathbf{r}_I,\omega)}{G_D(\mathbf{r}_I;\mathbf{r}_S,\omega)}\right] \quad (11)$$

and

$$K_U^F(\mathbf{r},\mathbf{r}_S,\mathbf{r}_I,\omega) = \mathrm{Im}\left[2k_0^2\frac{G_U^*(\mathbf{r};\mathbf{r}_S,\omega)G(\mathbf{r};\mathbf{r}_I,\omega)}{G_U^*(\mathbf{r}_I;\mathbf{r}_S,\omega)}\right] \quad (12)$$

are frequency-domain sensitivity or Fréchet kernels for source and receiver sides. Equations 8–12 give the relationship between the velocity perturbation and the phase delay in the depth image.

In the time or depth domain, the more convenient observations are broadband time delay or moveout. Thus, we convert the phase delay into a traveltime delay and use a crosscorrelation to define the time delay. Using the derivation in Appendix A, the broadband time delay can be expressed as a weighted average of traveltime delays of its harmonic contents:

$$\delta t = \int W(\omega)\delta t(\omega)d\omega, \quad (13)$$

where $W(\omega)$ is a normalized weighting function given in Appendix A. Notice that $\delta t(\omega) = \delta\varphi(\omega)/\omega$ is the time delay of individual harmonic waves. By substituting equations 8–12 into equation 13, the broadband time delay relating to the velocity perturbation can be expressed as

$$\delta t(\mathbf{r}_I,\mathbf{r}_S) = \delta t_D(\mathbf{r}_I,\mathbf{r}_S) + \delta t_U(\mathbf{r}_I,\mathbf{r}_S), \quad (14)$$

with

$$\delta t_D(\mathbf{r}_I,\mathbf{r}_S) = \int_V m(\mathbf{r}')K_D^B(\mathbf{r}',\mathbf{r}_S,\mathbf{r}_I)dV' \quad (15)$$

and

$$\delta t_U(\mathbf{r}_I,\mathbf{r}_S) = \int_V m(\mathbf{r}')K_U^B(\mathbf{r}',\mathbf{r}_S,\mathbf{r}_I)dV', \quad (16)$$

where

$$K_D^B(\mathbf{r},\mathbf{r}_S,\mathbf{r}_I) = \int \frac{W(\omega)}{\omega}K_D^F(\mathbf{r},\mathbf{r}_S,\mathbf{r}_I,\omega)d\omega \quad (17)$$

and

$$K_U^B(\mathbf{r},\mathbf{r}_S,\mathbf{r}_I) = \int \frac{W(\omega)}{\omega}K_U^F(\mathbf{r},\mathbf{r}_S,\mathbf{r}_I,\omega)d\omega \quad (18)$$

are broadband-time delay sensitivity kernels for the down- and upgoing sides, respectively. The broadband time delay depends on the specific measuring method. If a method other than the crosscorrelation is used, the weighting function $W(\omega)$ may be different. Equation 13 is similar to those used by Luo and Schuster (1991) and Dahlen et al. (2000).

To convert the traveltime delay into the RMO, we examine the wavefields near the image point. Figure 1 illustrates the imaging processes for different CIGs. For the offset-index CIG in Figure 1a, the source and receiver waves are spherical waves from point sources. For the angle-index CIG in Figure 1b, the source and receiver waves are decomposed into local plane waves. For the shot-index CIG in Figure 1c, the source wave comes from a point source but the receiver wave is a reconstructed reflection wave. Although different CIGs involve different wavefront shapes, these waves behave similarly when approaching the image point. We investigate acoustic waves, so the local propagation directions of the down- and upgoing waves, $\hat{\mathbf{e}}_D$ and $\hat{\mathbf{e}}_U$, form a pair of reflection angles that mirror each other regarding the normal vector $\mathbf{n}$.

In a migration process, the image is extracted at the image point at zero time. A temporal shift in the image can cause its spatial shift, and vice versa (e.g., Sava and Fomel, 2006). Figure 2 illustrates the trajectory of the image in the space-time domain. Near the imaging point, correct to the first order, the trajectory in the true model is parallel to the trajectory in the initial model. The horizontal separation between the two trajectories denotes traveltime (or phase) error, and the vertical separation is the observed RMO. The slope of the trajectory depends on the local wave velocity and the reflection angle (Sava and Fomel, 2006) and relates the observed RMO to the traveltime delay. In a general case where the two trajectories are not precisely parallel, this relationship is an approximation and iterations are required.

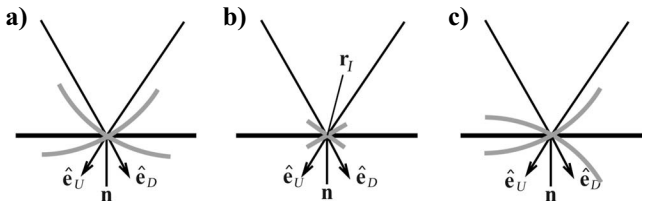

Figure 1. Imaging processes for different CIGs, where the thick solid line is the image of the target, the gray curves are down- and upgoing wavefronts, their crossing point is the imaging location, $\mathbf{n}$ is the normal vector to the target image, and $\hat{\mathbf{e}}_D$ and $\hat{\mathbf{e}}_U$ are unit vectors indicating the local propagation directions of the wavefields when approaching the imaging point. (a) Offset-index CIG; (b) angle-index CIG; and (c) shot-index CIG.

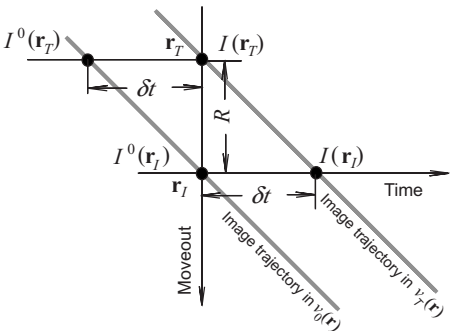

Figure 2. Relationship between the traveltime delay and the RMO. The horizontal coordinate is the temporal shift, and the vertical coordinate is the spatial shift along the reflector normal direction. Gray lines are the image trajectories in the true model and the initial model, respectively. The horizontal separation between the two trajectories denotes the traveltime delay, and the vertical separation is the observed RMO. The slope of the trajectory links the traveltime delay and the RMO.

Appendix B derives the relationship between the RMO and the traveltime delay:

$$R(\mathbf{r}_I,\mathbf{r}_S) = -\frac{v_0(\mathbf{r}_I)}{2\cos[\theta(\mathbf{r}_I,\mathbf{r}_S)]}\delta t(\mathbf{r}_I,\mathbf{r}_S), \quad (19)$$

where

$$R(\mathbf{r}_I,\mathbf{r}_S) = \mathbf{n}\cdot(\mathbf{r}_I-\mathbf{r}_T) = \mathbf{n}\cdot\mathbf{r}_{\mathrm{RMO}} \quad (20)$$

is the RMO measured along the reflector normal direction, $\delta t(\mathbf{r}_I,\mathbf{r}_S)$ is the corresponding traveltime delay, $v_0(\mathbf{r}_I)$ is the local velocity at $\mathbf{r}_I$, and $\theta(\mathbf{r}_I,\mathbf{r}_S)$ is the reflection angle relative to the reflector normal. Equation 19 is a local time-depth transform that converts the traveltime delay into the RMO with considerations of the local wave velocity, the oblique incidence of waves, and the reflector dip angle. This equation is similar to those obtained by Bishop et al. (1985) and Stork (1992) for offset-index CIG, and by Biondi and Symes (2004) and Sava and Fomel (2006) for angle-index CIG.

Figure 3 is a sketch showing the relationship between the reflection angle and the moveout. In practice, the RMO is often measured along the vertical direction rather than along the image normal. For a section of image with a dip angle α (Figure 3), the RMO along the normal direction can be obtained from the vertically measured RMO through the relationship

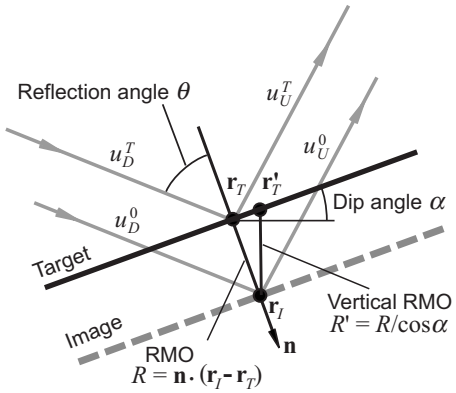

Figure 3. The relationship between the reflection angle, the dip angle, and the RMO. The thick solid line is the target, the gray dashed line is the image, and the thin gray lines are down- and upgoing waves.

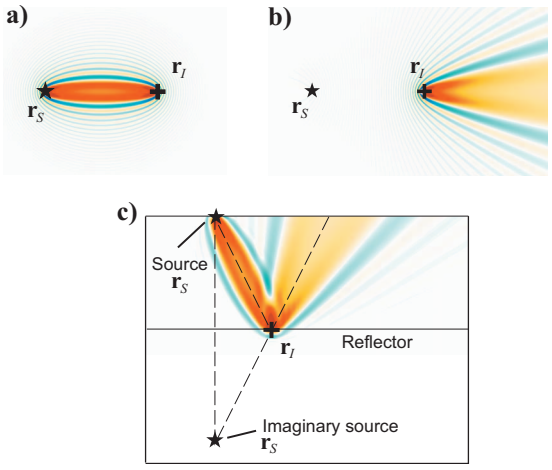

Figure 4. The construction of the broadband sensitivity kernel for prestack RMO: (a) the sensitivity kernel for the downgoing side, (b) the kernel for the upgoing side, and (c) the kernel formed by combining the down- and upgoing side kernels. The stars are sources, and the crosses are imaging points.

$$R = \mathbf{n}\cdot(\mathbf{r}_I-\mathbf{r}'_T) = R'\cos\alpha, \quad (21)$$

where R' is the vertically measured RMO and $\mathbf{r}'^T_T$ is a point on the target and vertically above the image point $\mathbf{r}_I$. Substituting equations 14–18 into equation 19, we have

$$R(\mathbf{r}_I,\mathbf{r}_S) = -\frac{v_0(\mathbf{r}_I)}{2\cos[\theta(\mathbf{r}_I,\mathbf{r}_S)]}\int_V m(\mathbf{r}')[K_D^B(\mathbf{r}',\mathbf{r}_S,\mathbf{r}_I) + K_U^B(\mathbf{r}',\mathbf{r}_S,\mathbf{r}_I)]dV', \quad (22)$$

which links the observed RMO to the perturbation $m(\mathbf{r})$ in a migration-velocity model.

In equation 22, the broadband sensitivity kernel is composed of two terms: one for the downgoing side and one for the upgoing side. Together, they form a weighting function that determines how the migration RMO senses the errors in the velocity model. For a further understanding of the individual terms in the sensitivity kernel, Figure 4 schematically demonstrates the construction of this kernel. Shown in Figure 4a is the source-side kernel $K_D^B(\mathbf{r}',\mathbf{r}_S,\mathbf{r}_I)$, which is similar to a conventional sensitivity kernel for a transmitted wave from a point source to a point receiver (here, replaced by the image point $\mathbf{r}_I$). With reference to equations 11 and 17, this kernel involves the crosscorrelation between two Green's functions: one from the source and one from the image point. The sensitivity is distributed mainly between the source and the image point.

What is unconventional is the upgoing side kernel $K_U^B(\mathbf{r}',\mathbf{r}_S,\mathbf{r}_I)$. This kernel, similar to the downgoing side, also involves the crosscorrelation between two Green's functions (see equations 12 and 18). However, because the imaging process involves a time-reversed reflection wave, i.e., the complex conjugate $G_U^*(\mathbf{r};\mathbf{r}_S,\omega)$ in equation 12, the crosscorrelation generates a different kernel. Shown in Figure 4b is the sensitivity kernel for a time-reversed source wave. Interestingly, instead of lying between the source and image point, the kernel is distributed in the opposite direction from the source. Taking a simple scenario of a flat reflector in a constant velocity and assuming that the reflectivity is in unity, the reflection wave can be viewed as emitted from an imaginary source below the reflector (Figure 4c). Using the kernel in Figure 4a for the downgoing side (the primary source and the image point) and using the kernel in Figure 4b for the upgoing side (the imaginary source and the image point), we obtain the sensitivity kernel for the prestack RMO (Figure 4c).

The above example is only for demonstration. When calculating a sensitivity kernel in actuality, a reflection wave should be used.

DIRECT SENSITIVITY MEASUREMENT AND VALIDATION OF THE BROADBAND SENSITIVITY KERNEL

To validate the theoretically derived broadband sensitivity kernel, we develop a method that directly measures the sensitivity of the migration RMO to variations in migration-velocity models. We start with a simple scenario by generating a 2D synthetic shot-record data set in a model with a constant background velocity and a horizontal reflector (Figure 5). We conduct depth migrations using this data set.

To introduce a velocity error in the migration velocity model, we add a small, circular trial-velocity perturbation in the original constant-velocity model. The trial perturbation (shown as a small solid circle in Figure 5b) has a diameter of 200 m and a velocity perturbation of 5%. For each migration, we measure the RMO from an image point located at a horizontal distance of 2.75 km. Given the velocity model and acquisition geometry, this measurement reveals how the RMO at the image point can sense the velocity variation at a particular location in the model. We move this trial perturbation and use it to scan the entire model. At each scanning point, we conduct a migration and measure the RMO using the crosscorrelation method. Finally, we use these RMO records to generate a sensitivity map for the entire model space.

Figure 5 compares the theoretically calculated broadband sensitivity kernel and the directly measured sensitivity map. Figure 5a is the broadband sensitivity kernel calculated with equation 22. The source is a 10-Hz Ricker wavelet, and the Green's function is calculated using the one-way propagator and multiple-forward-scattering and single-backscattering approximation (Xie and Wu, 2001; Wu et al., 2006). The model parameters are the ones we used to generate the synthetic data set. Shown in Figure 5b is the directly measured sensitivity map using the above-mentioned method, where each pixel is generated from a depth migration. We used 8000 migrations to generate this figure.

The general consistency between the two figures indicates that the theoretical kernel satisfactorily predicts the relationship between the RMO measurements and the variations in the migration-velocity model. The source-side sensitivity kernel is similar to the conventional Fréchet kernel for a wave transmitted from the source to the image point. However, the receiver-side kernel, which has a large upward opening, is quite different. Near the source location and immediately above the image point are two sensitive regions where the velocities strongly affect the RMO. Regions along the center of these kernels, i.e., where the traditional raypath is, show weaker sensitivity (for a 3D model, the sensitivities in these regions should be nearly zero [Woodward, 1992]). The main lobes of both down- and upgoing kernels are red, indicating that positive velocity perturbations in these regions cause positive RMOs (negative delay times). These regions are the first Fresnel zones. Around these red regions are blue regions where positive velocity perturbations can cause negative RMOs (positive delay times). The result shows a complex sensitivity distribution even for such a simple scenario. The regions within which the velocity can affect the RMO are much broader than that predicted by high-frequency rays, indicating that conventional ray-based methods may encounter difficulty in velocity updating.

THE INVERSION SYSTEM

Equation 22 creates a relationship between the observed RMO and the velocity errors in the migration-velocity model. It can be used as the basis for migration-velocity updating. However, the absolute RMO measurement is often unavailable in reality. Instead, the data we observe directly are relative RMOs between different shots. They often appear as curvatures in the CIGs.

Figure 6 illustrates the relationship between the absolute and relative RMOs. The relative RMO between two shots at $\mathbf{r}_{S1}$ and $\mathbf{r}_{S2}$ can be expressed as

$$\delta R(\mathbf{r}_{S1},\mathbf{r}_{S2},\mathbf{r}_I) = R(\mathbf{r}_{S2},\mathbf{r}_I) - R(\mathbf{r}_{S1},\mathbf{r}_I), \qquad (23)$$

Where $\delta R(\mathbf{r}_{S1},\mathbf{r}_{S2},\mathbf{r}_I)$ is the relative RMO between the two shots within the same CIG. Substituting equation 22 into equation 23, the relative RMO can be expressed as

$$\delta R(\mathbf{r}_{S1},\mathbf{r}_{S2},\mathbf{r}_I) = -\int_V m(\mathbf{r}')K^B(\mathbf{r}',\mathbf{r}_{S1},\mathbf{r}_{S2},\mathbf{r}_I)dV', \qquad (24)$$

where

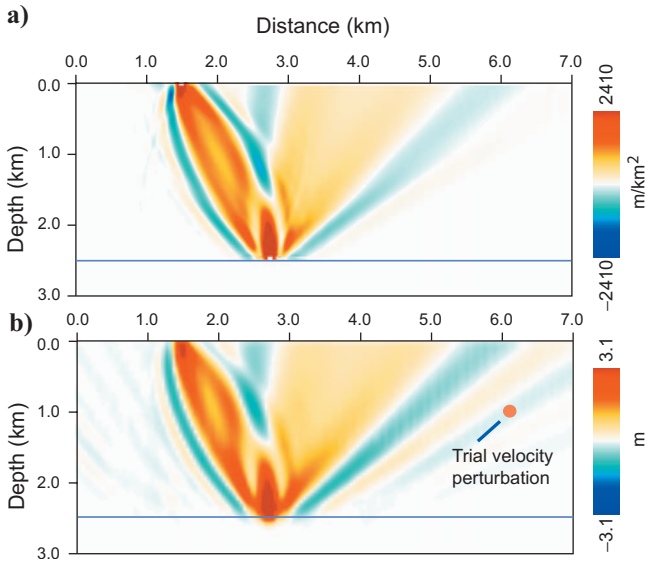

Figure 5. A sensitivity kernel for a shot-gather image: (a) the theoretical sensitivity kernel and (b) the sensitivity map directly measured from migration imaging. The background velocity is 3.0 km/s, and the depth of the reflector is 2.5 km. The source is located at the surface and at a horizontal distance of 1.5 km. The trial perturbation, shown as a small solid circle in (b), has a diameter of 200 m and a velocity perturbation of 5%. The receivers cover the entire surface of the model. Red indicates that positive-velocity perturbations in these regions cause positive (downward) RMOs. These regions are the first Fresnel zones. Blue indicates where positive velocity perturbations can cause negative RMOs.

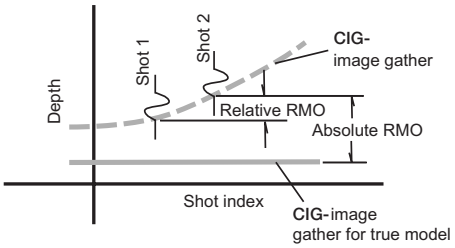

Figure 6. The relative RMO measurement from a pair of shots. The horizontal coordinate is the shot index, and the vertical coordinate is the RMO. The solid gray line is the unknown CIG in the true velocity model, and the dashed gray line is the observed CIG in the initial model.

$$K^B(\mathbf{r},\mathbf{r}_{S1},\mathbf{r}_{S2},\mathbf{r}_I) = \frac{v_0(\mathbf{r}_I)}{2\cos[\theta(\mathbf{r}_{S2},\mathbf{r}_I)]} \times [K_D^B(\mathbf{r},\mathbf{r}_{S2},\mathbf{r}_I) + K_U^B(\mathbf{r},\mathbf{r}_{S2},\mathbf{r}_I)] - \frac{v_0(\mathbf{r}_I)}{2\cos[\theta(\mathbf{r}_{S1},\mathbf{r}_I)]} \times [K_D^B(\mathbf{r},\mathbf{r}_{S1},\mathbf{r}_I) + K_U^B(\mathbf{r},\mathbf{r}_{S1},\mathbf{r}_I)] \quad (25)$$

is the broadband differential kernel that combines the sensitivities from a pair of shots in a CIG.

Figure 7 compares the theoretically calculated and the measured-broadband differential sensitivities in a 2D heterogeneous model. The source is a 17.5-Hz Ricker wavelet, and the velocity model has approximately 30% velocity variation. Figure 7a shows the differential sensitivity kernel calculated with equation 25. The one-way propagator, multiple-forward-scattering, and single-backscattering approximation are used in the calculation. Note the complex features resulting from a positive and a negative kernel. Figure 7b shows the sensitivity map measured directly from the migration imaging with the method mentioned in the previous section. The consistency between the theoretically calculated and directly measured sensitivities further confirms the validity of this kernel.

To build an inversion system, we partition the velocity model and the broadband kernel in equations 24 and 25 to generate the linear system:

$$\delta R(\mathbf{r}_{S1},\mathbf{r}_{S2},\mathbf{r}_I) = -\sum_i m(\mathbf{r}_i) K^B(\mathbf{r}_i,\mathbf{r}_{S1},\mathbf{r}_{S2},\mathbf{r}_I), \quad (26)$$

where

$$K^B(\mathbf{r}_i,\mathbf{r}_{S1},\mathbf{r}_{S2},\mathbf{r}_I) = \frac{v_0(\mathbf{r}_I)}{2\cos[\theta(\mathbf{r}_{S2},\mathbf{r}_I)]} \times [K_D^B(\mathbf{r}_i,\mathbf{r}_{S2},\mathbf{r}_I) + K_U^B(\mathbf{r}_i,\mathbf{r}_{S2},\mathbf{r}_I)] - \frac{v_0(\mathbf{r}_I)}{2\cos[\theta(\mathbf{r}_{S1},\mathbf{r}_I)]} \times [K_D^B(\mathbf{r}_i,\mathbf{r}_{S1},\mathbf{r}_I) + K_U^B(\mathbf{r}_i,\mathbf{r}_{S1},\mathbf{r}_I)] \quad (27)$$

and where

$$K_D^B(\mathbf{r}_i,\mathbf{r}_S,\mathbf{r}_I) = \int_{V(\mathbf{r}_i)} K_D^B(\mathbf{r}',\mathbf{r}_S,\mathbf{r}_I)dV' \quad (28)$$

and

$$K_U^B(\mathbf{r}_i,\mathbf{r}_S,\mathbf{r}_I) = \int_{V(\mathbf{r}_i)} K_U^B(\mathbf{r}',\mathbf{r}_S,\mathbf{r}_I)dV' \quad (29)$$

are discretized broadband kernels. The value $V(\mathbf{r}_i)$ is a subspace of V and is indexed by its location $\mathbf{r}_i$, and $m(\mathbf{r}_i)$ is the unknown velocity perturbation at the partitioned subspace. In equations 26–29, $(\mathbf{r}_{S1},\mathbf{r}_{S2},\mathbf{r}_I)$ is the index for relative RMO data, and $(\mathbf{r}_i)$ is the index for unknown velocity perturbations.

Once we have the relative RMO data $\delta R(\mathbf{r}_{S1},\mathbf{r}_{S2},\mathbf{r}_I)$ and the differential kernel $K^B(\mathbf{r}_i,\mathbf{r}_{S1},\mathbf{r}_{S2},\mathbf{r}_I)$ calculated from the initial model $v_0(\mathbf{r})$, we can use equation 26 to invert the velocity perturbation $m(\mathbf{r}_i)$. The resulting velocity perturbations can be used to update the velocity model and to improve image quality.

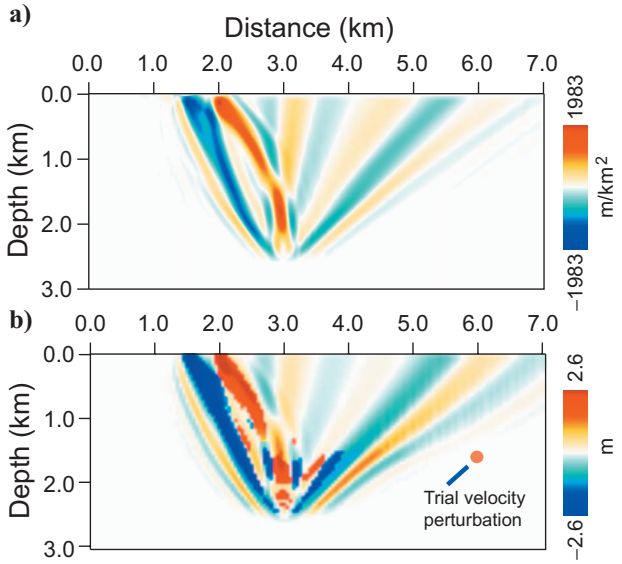

Figure 7. A broadband-differential sensitivity kernel for a variable-background velocity model: (a) the theoretical kernel and (b) the measured sensitivity map. The trial perturbation, shown as a small solid circle in (b), has a diameter of 200 m and a velocity perturbation of 5%. Note the complex sensitivity distribution caused by a positive and a negative kernel.

NUMERICAL EXAMPLES

We present two simple numerical examples to demonstrate the potential applications of the broadband sensitivity kernel in MVA. In these calculations, all synthetic data sets are generated with a fourth-order scalar-wave finite-difference method. The migration is conducted by a local cosine-based one-way propagator (Luo et al., 2004). The RMO is measured using crosscorrelation between traces. The broadband sensitivity kernels are calculated in the initial model using the method described above.

To calculate the reflection wave, we need the location of the reflector determined from the depth image in the initial model. To determine the reflection angle $\theta(\mathbf{r}_I,\mathbf{r}_S)$, we measure the dip angle from the image in the initial model and calculate the propagation direction of the source wave using the method of Xie and Wu (2002). Calculating the reflection angle $\theta(\mathbf{r}_I,\mathbf{r}_S)$ requires information from only the initial model and can be done while calculating the sensitivity kernels. We use a grid-cell model to partition the velocity perturbation and the broadband sensitivity kernel. We then substitute these data into equation 26 and build an inversion system. The least-squares method by Lawson and Hanson (1974) is used to solve the linear system.

Inversion in a constant-background velocity model

Figure 8 shows the inversion in a constant-background velocity model. The true velocity model in Figure 8a is composed of a constant background and a horizontal reflector. Four Gaussian-shaped velocity perturbations are located near the center of the model. Their different sizes are used to test the resolution of the inversion. Figure 8b shows the locations of the nine sources for generating the data set. The synthetic data are calculated using a 17.5-Hz Ricker wavelet,

and the receivers cover the entire model surface. Seventeen image points are used to measure the RMO. Figure 8b also shows the discretized velocity perturbations used to check the inversion result.

We target our inversion within a 1.5×1.5-km region with the rest of the model unperturbed. A 0.3×0.3-km block size is used to partition the sensitivity kernel and unknown velocity perturbations. We conduct the migration in the background velocity model. The RMOs are measured from the shot-index CIGs and used for inversion. The inverted velocity perturbations are shown in Figure 8c. Comparing Figure 8c with Figure 8b, we see the inverted velocity perturbations recover the main feature of the model.

Inversion in a variable-background velocity model

Our second example tests the inversion in a variable-background velocity model. The true velocity model shown in Figure 9a is composed of two parts: the background velocity in Figure 9b and the checkerboard-shaped velocity perturbations in Figure 9c. The background velocity varies between 3.0 and 4.1 km/s. The velocity perturbations have a maximum $\pm 5\%$ variation.

A horizontal reflector is located at a depth of 2.5 km. Eight shots are used to generate synthetic data sets, and the RMOs are measured from eight image points. The locations for sources and image points are shown in Figure 9c. The synthetic data set is calculated in the true velocity model using a 17.5-Hz Ricker wavelet. The migration is calculated in the background velocity model, and the RMOs are measured from the shot-index CIGs. We limit our inversion within the dashed rectangle shown in Figure 9c. The broadband kernel and the unknown perturbations are partitioned similar to the checkerboard. Illustrated in Figure 9d are inverted velocity perturbations that recover the checkerboard pattern of the original velocity perturbations.

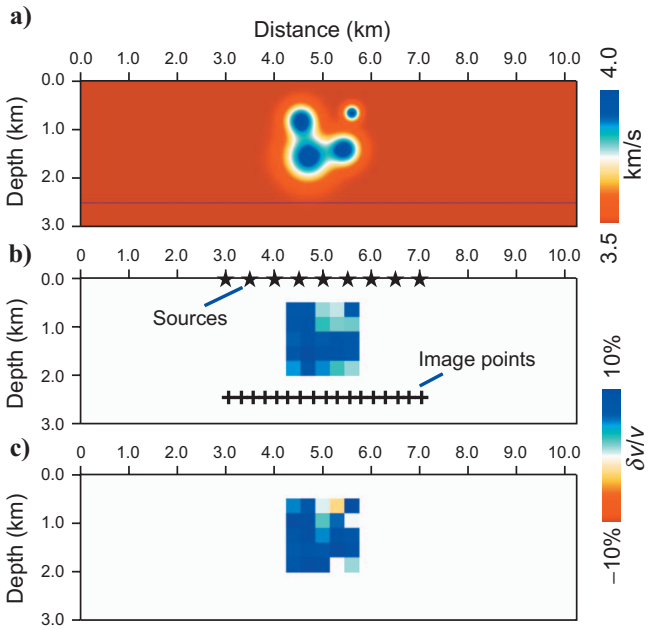

Figure 8. Inversion for a constant background velocity model, where (a) is the true velocity model, (b) is the descretized velocity perturbation, and (c) is the inverted velocity perturbation. The true velocity model is composed of a 3.5-km/s background velocity plus four Gaussian velocity perturbations located near the center of the model. Their different sizes are used to test the resolution of the inversion, and the maximum velocity perturbation is $+10\%$ at the centers of these patches. A horizontal reflector is located at a depth of 2.5 km. During inversion, the model is partitioned using 0.3×0.3 km grid cells.

DISCUSSION

The sensitivity-kernel-based velocity analysis we propose is a wave-equation method that considers wave phenomena, e.g., finite frequency, scattering, diffraction, and multipathing. However, there are differences between this method and some full-wave-equation-based MVAs. The information for velocity updating includes amplitude and moveout in the CIGs. Although the depth image itself is generated by the backscattered waves that largely sense the sharp variations in the model, the RMO (equivalent to the traveltime delay in seismograms) is formed mostly by the accumulated forward-scattering waves along the propagation path. This information mainly senses the large-scale perturbations in the velocity models. The amplitude information linked to the focusing/defocusing effect is more sensitive to the small- to medium-sized heterogeneities.

Many full-wave-equation-based methods deal with kinematics and dynamic information that should provide better constraints on velocity perturbations of all scales. However, the application of dynamic information also relies on accurate initial models, a true-amplitude wave propagator, and high-fidelity data. Otherwise, it may cause convergence difficulties in the inversion process. Considering that the primary purpose of the MVA is to update the large-scale

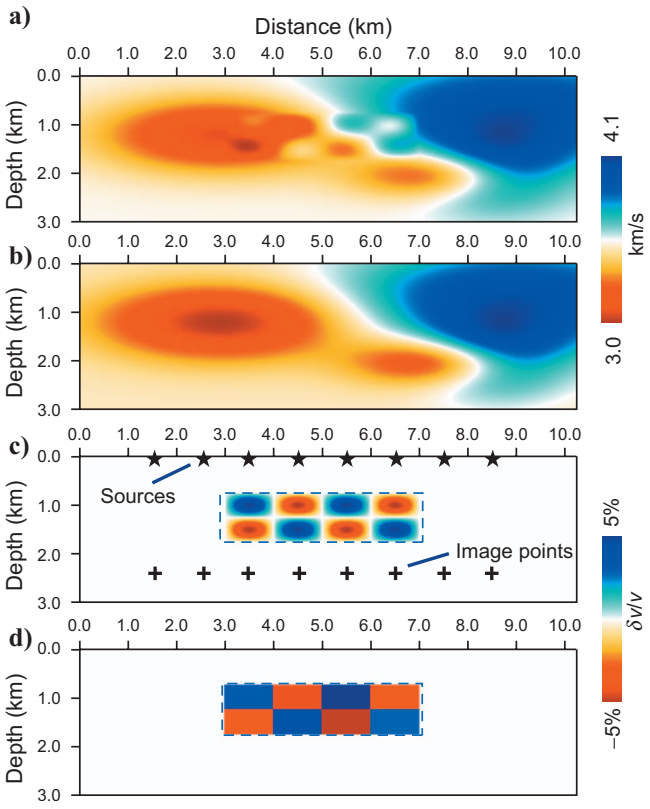

Figure 9. Inversion for a variable background model: (a) true velocity model, (b) background velocity model, (c) velocity perturbations, and (d) inverted perturbations. The background velocity varies between 3.0 and 4.1 km/s. The velocity perturbations have maximum $\pm 5\%$ variations overlapped on the background velocity. A horizontal reflector is located at a depth of 2.5 km.

background velocity model, we avoid using the amplitude information in our method. This allows a more robust method, able to tolerate larger errors in the initial models. However, it comes at some cost in resolution.

The current method shares many similarities with the ray-based velocity-analysis method. Both methods use the same RMO data, which sense the large-scale velocity perturbations. The major difference between the two methods is that the ray-based method is derived from the high-frequency asymptotic approximation. It backprojects the corrections to a velocity model along thin rays. When a band-limited seismic wave is used, the rays do not approximate the actual wavepaths accurately. Our new method maps the velocity corrections to the model through sensitivity kernels derived from the wave theory. The actually measured sensitivity maps (Figures 5b and 7b) clearly reveal that the sensitivity kernels are more accurate than rays. In addition, the sensitivity kernels are volumetric. They provide better coverage in the model, particularly in some poorly illuminated regions.

CONCLUSIONS

We derive a broadband sensitivity kernel relating the RMO in PSDM to the velocity variations in a migration velocity model. The new method is formulated for the shot-record PSDM and shot-index CIG. Thus, no expensive angle-domain analysis is required. Based on this sensitivity kernel, we build an inversion system that converts the observed RMO to the correction in the migration velocity model. An efficient method based on the one-way propagator and multiple forward-scattering and single backscattering approximation is used to calculate sensitivity kernels. We also designed a method to measure the sensitivity map directly from the migration process. The consistency between the broadband sensitivity kernel and the measured sensitivity map validates our theory and the numerical implementations.

Finally, synthetic data sets are used to test the inversion system. This is a wave-equation method that naturally incorporates the wave phenomena and is best teamed with the wave-equation-based migration method for velocity analysis. This method still maintains the simplicity of a ray-based velocity-analysis method, although the rays are replaced with the more accurate sensitivity kernels.

Our principal purpose has been to present the broadband sensitivity kernel for the RMO. Numerical examples are used to validate the theory and demonstrate the potential applications of this method. All calculations have been conducted close to the linear condition. For a more general case, where the initial model is strongly biased relative to the true-velocity model, linearization and iterations are required. The current numerical examples are for 2D models. However, there is no major obstacle to generalizing these calculations to 3D problems.

ACKNOWLEDGMENTS

The authors thank Frank Adler and two anonymous reviewers for valuable comments that greatly improved this manuscript. This research is supported by the DOE/BES project at the University of California, Santa Cruz under grant DE-FG02-04ER15530. Facility support from the W. M. Keck Foundation is also gratefully acknowledged.

APPENDIX A

BROADBAND TRAVELTIME DELAY

Given that the signal we are interested in is slightly dispersive but still impulsive (unlike highly dispersive surface waves), we use the crosscorrelation to define the time shift of a broadband signal relative to a reference signal. Assuming the two signals have similar waveforms and thus similar frequency contents, their crosscorrelation function can be expressed as (Båth, 1974)

$$c(t) = \int S(\omega)S^*(\omega)e^{i\omega\delta t(\omega)}e^{-i\omega t}d\omega, \qquad \text{(A-1)}$$

where $S(\omega)$ is the Fourier spectrum of the reference signal, $S(\omega)e^{i\omega\delta t(\omega)}$ is the Fourier spectrum of the signal to be measured, and

$$\delta t(\omega) = \frac{\delta\varphi(\omega)}{\omega} \qquad \text{(A-2)}$$

is the time delay of individual harmonic waves. We determine the relative time shift of the broadband signal by measuring the time shift of the maximum correlation in $c(t)$. To do this, we calculate

$$\left.\frac{\partial c(t)}{\partial t}\right|_{t=\delta t} = -i\int \omega P(\omega)e^{i\omega[\delta t(\omega)-\delta t]}d\omega = 0, \qquad \text{(A-3)}$$

where δt is the broadband time delay to be determined and $P(\omega) = S(\omega)S^*(\omega)$ is the power spectrum of the signal. Because the dispersion $\delta t(\omega) - \delta t$ is very small, we apply the Taylor expansion to the exponential function and have

$$-i\int \omega P(\omega)d\omega + \int \omega^2 P(\omega)\delta t(\omega)d\omega - \delta t\int \omega^2 P(\omega)d\omega = 0. \qquad \text{(A-4)}$$

The value ω is an odd function and the power spectrum $P(\omega)$ is an even function, and the first integral in equation A-4 is zero. Solving this equation gives the broadband time delay

$$\delta t = \int W(\omega)\delta t(\omega)d\omega, \qquad \text{(A-5)}$$

where

$$W(\omega) = \frac{\omega^2 P(\omega)}{\int \omega^2 P(\omega)d\omega} \qquad \text{(A-6)}$$

is a normalized weighting function relating to the power spectrum. Equation A-6 shows that the broadband time delay is a weighted average of time delays of its harmonic contents.

APPENDIX B

RELATIONSHIP BETWEEN TRAVELTIME DELAY AND RMO

To obtain the relationship between the traveltime delay and the observed RMO, we expand the imaging condition near the image location $\mathbf{r}_I$ to the first order:

$$I(\mathbf{r},t) = I_0\delta[T_D(\mathbf{r}) - t_D]\delta[T_U(\mathbf{r}) - t_U] = I_0\delta[T_D(\mathbf{r}) + T_U(\mathbf{r}) - t], \quad \text{(B-1)}$$

where $I(\mathbf{r},t)$ is the space-time domain image, I_0 is the amplitude that is a slowly varying function of space, $\delta(\cdot)$ is Dirac's delta function, $T_D(\mathbf{r}) = 0$ and $T_U(\mathbf{r}) = 0$ are wavefront equations for the down- and upgoing waves, and $t = t_D + t_U$ is the two-way traveltime delay. We then calculate

$$dI = \frac{\partial I}{\partial t}\delta t + \nabla I \cdot (\mathbf{r} - \mathbf{r}_I) = 0 \quad \text{(B-2)}$$

near the image location. Note that

$$\frac{\partial I}{\partial t}\delta t = -I'\,\delta t \quad \text{(B-3)}$$

and

$$\nabla I \cdot (\mathbf{r} - \mathbf{r}_I) = I'\,[\nabla T_D(\mathbf{r}) + \nabla T_U(\mathbf{r})]\big|_{\mathbf{r}=\mathbf{r}_I} \cdot (\mathbf{r} - \mathbf{r}_I). \quad \text{(B-4)}$$

Following Aki and Richards (1980, p. 90), the gradients

$$\nabla T_D(\mathbf{r})\big|_{\mathbf{r}=\mathbf{r}_I} = \frac{\hat{\mathbf{e}}_D}{v_0} \quad \text{(B-5)}$$

and

$$\nabla T_U(\mathbf{r})\big|_{\mathbf{r}=\mathbf{r}_I} = \frac{\hat{\mathbf{e}}_U}{v_0} \quad \text{(B-6)}$$

are local slowness vectors of the down- and upgoing waves at the imaging point. Substituting equations B-3–B-6 into B-2, we have

$$(\hat{\mathbf{e}}_D + \hat{\mathbf{e}}_U) \cdot (\mathbf{r} - \mathbf{r}_I) = v_0(\mathbf{r}_I)\delta t. \quad \text{(B-7)}$$

Noting that $\hat{\mathbf{e}}_D + \hat{\mathbf{e}}_U = 2\cos\theta\mathbf{n}$, we have the relationship between the RMO and the traveltime delay

$$\mathbf{n} \cdot (\mathbf{r}_I - \mathbf{r}) = -\frac{v_0(\mathbf{r}_I)}{2\cos\theta}\delta t. \quad \text{(B-8)}$$

REFERENCES

Aki, K., and P. G. Richards, 1980, Quantitative seismology: Theory and methods I: W. H. Freeman & Co.

Al-Yahya, K. A., 1989, Velocity analysis by iterative profile migration: Geophysics, **54**, 718–729.

Båth, M., 1974, Spectral analysis in geophysics: Elsevier Science Publ. Co., Inc.

Biondi, B., 2006, 3D seismic imaging: SEG.

Biondi, B., and W. W. Symes, 2004, Angle-domain common-image gathers for migration velocity analysis by wavefield-continuation imaging: Geophysics, **69**, 1283–1298.

Bishop, T. N., K. P. Bube, R. T. Cutler, R. T. Langan, P. L. Love, J. R. Resnick, R. T. Shuey, D. A. Spindler, and H. W. Wyld, 1985, Tomographic determination of velocity and depth in laterally varying media: Geophysics, **50**, 903–923.

Buursink, M. L., and P. S. Routh, 2007, Application of borehole-radar Fresnel volume tomography to image porosity in a sand and gravel aquifer: 77th Annual International Meeting, SEG, Expanded Abstracts, 668–672.

Chauris, H., and M. Noble, 2001, Two-dimensional velocity macro model estimation from seismic reflection data by local differential semblance optimization: Applications to synthetic and real data sets: Geophysical Journal International, **144**, 14–26.

Chen, P., L. Zhao, and T. H. Jordan, 2007, Full 3D tomography for the crustal structure of the Los Angeles region: Bulletin of the Seismological Society of America, **97**, 1094–1120.

Dahlen, F., 2005, Finite-frequency sensitivity kernels for boundary topography perturbations: Geophysical Journal International, **162**, 525–540.

Dahlen, F., S. Huang, and G. Nolet, 2000, Fréchet kernels for finite-frequency traveltimes — I: Theory: Geophysical Journal International, **141**, 157–174.

de Hoop, M. V., R. D. van der Hilst, and P. Shen, 2006, Wave equation reflection tomography: Annihilators and sensitivity kernels: Geophysical Journal International, **167**, 1332–1352.

Fliedner, M. M., M. P. Brown, D. Bevc, and B. Biondi, 2007, Wave path tomography for subsalt velocity model building: 77th Annual International Meeting, SEG, Expanded Abstracts, 1938–1942.

Huang, S., F. Dahlen, and G. Nolet, 2000, Fréchet kernels for finite-frequency traveltimes — II, Examples: Geophysical Journal International, **141**, 175–203.

Jocker, J., J. Spetzler, D. Smeulders, and J. Trampert, 2006, Validation of first-order diffraction theory for the traveltimes and amplitudes of propagating waves: Geophysics, **71**, no. 6, T167–T177.

Khoury, A., W. Symes, P. Williamson, and P. Shen, 2006, DSR migration velocity analysis by differential semblance optimization: 76th Annual International Meeting, SEG, Expanded Abstracts, 2450–2454.

Lawson, C. L., and R. J. Hanson, 1974, Solving least squares problems: Prentice-Hall, Inc.

Liu, Z., and N. Bleistein, 1992, Velocity analysis by residual moveout: 62nd Annual International Meeting, SEG, Expanded Abstracts, 1024–1037.

Luo, M., R. S. Wu, and X. B. Xie, 2004, Beamlet migration using local cosine basis with shifting windows: 74th Annual International Meeting, SEG, Expanded Abstracts, 945–948.

Luo, Y., and G. T. Schuster, 1991, Wave-equation traveltime tomography: Geophysics, **56**, 645–653.

Mosher, C., and D. Foster, 2000, Common angle imaging conditions for prestack depth migration: 70th Annual International Meeting, SEG, Expanded Abstracts, 830–833.

Mosher, C., S. Jin, and D. Foster, 2001, Migration velocity analysis using common angle image gathers: 71st Annual International Meeting, SEG, Expanded Abstracts, 889–892.

Prucha, M., B. Biondi, and W. Symes, 1999, Angle-domain common image gathers by wave-equation migration: 69th Annual International Meeting, SEG, Expanded Abstracts, 824–827.

Rickett, J. E., and P. C. Sava, 2002, Offset and angle-domain common image point gathers for shot-profile migration: Geophysics, **67**, 883–889.

Sava, P. C., and B. Biondi, 2004, Wave-equation migration velocity analysis — I: Theory: Geophysical Prospecting, **52**, 593–606.

Sava, P. C., and S. Fomel, 2003, Angle-domain common-image gathers by wavefield continuation methods: Geophysics, **68**, 1065–1074.

———, 2006, Time-shift imaging condition in seismic migration: Geophysics, **71**, no. 6, S209–S217.

Shen, P., W. Symes, and C. Stolk, 2003, Differential semblance velocity analysis by wave-equation migration: 73rd Annual International Meeting, SEG, Expanded Abstracts, 2135–2139.

Skarsoulis, E. K. and B. D. Cornuelle, 2004, Travel-time sensitivity kernels in ocean acoustic tomography: Journal of the Acoustical Society of America, **116**, 227–238.

Soubaras, R., and B. Gratacos, 2007, Velocity model building by semblance maximization of modulated-shot gathers: Geophysics, **72**, no. 5, U67–U73.

Spetzler, J., and R. Snieder, 2004, The Fresnel volume and transmitted waves: Geophysics, **69**, 653–663.

Stork, C., 1992, Reflection tomography in the postmigrated domain: Geophysics, **57**, 680–692.

Symes, W., and J. Carazzone, 1991, Velocity inversion by differential semblance optimization: Geophysics, **56**, 654–663.

Vasco, D. W., J. E. Peterson Jr., and E. L. Majer, 1995, Beyond ray tomography: Wavepaths and Fresnel volumes: Geophysics, **60**, 1790–1804.

Woodward, M. J., 1992, Wave-equation tomography: Geophysics, **57**, 15–26.

Wu, R. S., X. B. Xie, and X. Y. Wu, 2006, One-way and one-return approximations (de Wolf approximation) for fast elastic wave modeling in complex media, *in* R. S. Wu and V. Maupin, eds., Advances in wave propagation in heterogeneous earth: Elsevier Science Publ. Co., Inc., 265–322.

Xie, X. B., and R. S. Wu, 2001, Modeling elastic wave forward propagation and reflection using the complex screen method: Journal of the Acoustical Society of America, **109**, 2629–2635.

———, 2002, Extracting angle domain information from migrated wavefield: 72nd Annual International Meeting, SEG, Expanded Abstracts, 1360–1363.

Zhao, L., T. H. Jordan, and C. H. Chapman, 2000, Three-dimensional Fréchet differential kernels for seismic delay times: Geophysical Journal International, **141**, 558–576.